ACS APPLIED MATERIALS & INTERFACES

www.acsami.org

Research Article

Stoner Ferromagnetism in Hole-Doped $CuM^{IIIA}O_2$ with M^{IIIA} = Al, Ga, and In

Konstantina Iordanidou* and Clas Persson

Cite This: *ACS Appl. Mater. Interfaces* 2021, 13, 29770–29779

Read Online

ACCESS | Metrics & More | Article Recommendations | Supporting Information

ABSTRACT: Using density functional theory calculations, we examine the effect of hole doping on the magnetic and electronic properties of $CuM^{IIIA}O_2$, with M^{IIIA} = Al, Ga, and In. $CuM^{IIIA}O_2$ nonmagnetic semiconductors switch to ferromagnetic half-metals upon hole doping. For $CuAlO_2$, the nonmagnetic-to-ferromagnetic transition occurs for hole densities of $\sim 7 \times 10^{19}/cm^3$. Ferromagnetism arises from an exchange splitting of the electronic states at the valence band edge, and it can be attributed to the high-lying Cu-d states. Hole doping induced by cation vacancies and substitutional divalent dopants is also investigated. Interestingly, both vacancies and nonmagnetic divalent dopants result in the emergence of ferromagnetism.

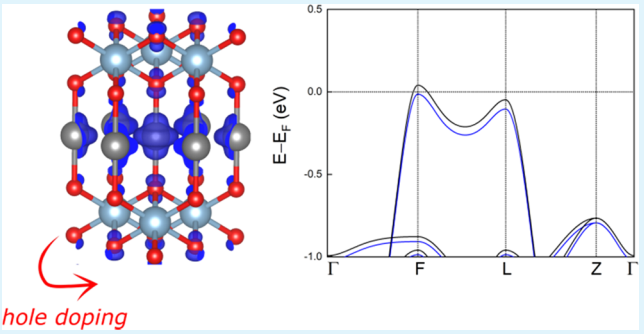

KEYWORDS: *$CuAlO_2$, hole doping, defects, ferromagnetism, first-principles*

1. INTRODUCTION

Ferromagnets such as iron, cobalt, and nickel, are typically metals, whereas materials with both ferromagnetic and semiconducting properties are scarce. Ferromagnetic semiconductors are attractive candidates for future spintronic devices, owing to their easy integration into the existing semiconductor devices.[1] Over the past few decades, diluted magnetic semiconductors (DMS), i.e., nonmagnetic semiconductors doped with magnetic ions, have triggered intense interest.[2−5] Magnetic moments mainly arise from partially filled 3d and 4f orbitals of transition metals and rare earth metals, and examples of DMS include (Ga,Mn)As, (Zn,Cr)Se, and (Pb,Eu)Te. Although $Ga_{1-x}Mn_xAs$ has been one of the most widely studied DMS, its low Curie temperature hinders its utilization in practical applications. Contrary to GaAs-based DMS, room-temperature ferromagnetism has been observed in diluted magnetic oxides such as TiO_2, ZnO, and SnO.[6−10] Intriguingly, high-temperature ferromagnetism in the absence of magnetic ions has been additionally reported.[11−21] For instance, Kenmochi et al. found that carbon-doped oxides such as MgO, SrO, BaO, and CaO are ferromagnetic without any transition-metal impurities, and based on the mean-field approximation, Curie temperatures higher than room temperature have been predicted.[19−21]

Two types of diluted magnetic semiconductors with different properties have been widely studied. First, for DMS like Mn-doped GaSb with localized majority d-states deep in the valence band, ferromagnetism arises from the Zener's p−d exchange mechanism, resulting in holes in the majority p-valence band. Such interaction is relatively weak and long-range, and the Curie temperature scales linearly with the impurity concentration. On the other hand, for DMS like Mn-doped GaN with impurity bands within the band gap, ferromagnetism arises from the Zener's double-exchange mechanism. The magnetic couple is strong and short-ranged, and the Curie temperature scales proportionally to the square root of the impurity concentration.[22,23]

Doping of $CuAlO_2$ with magnetic ions such as Mn, Fe, and Co, to form oxide-based DMS, has been intensively investigated.[24−27] For instance, first-principles calculations revealed that (Cu,Fe)AlO_2 and (Cu,Co)AlO_2 are attractive candidates as high-Tc ferromagnets. Overall, $CuAlO_2$ is an attractive candidate for various applications owing to its p-type conductivity (without intentional doping) and its visible light transparency.[28−30] In general, the design of p-type transparent conductive oxides (TCO) is found to be difficult, and the difficulty arises from the nature of the VB edge, dominated by localized O-2p states.[31,32] Holes are typically trapped at O sites and cannot migrate through the oxide, leading to poor p-type behavior. To overcome this limitation, modulation of the VB edge through hybridization of the O-2p orbitals with metal orbitals has been proposed.[31] The discovery of p-type

Received: January 11, 2021
Accepted: May 11, 2021
Published: June 21, 2021

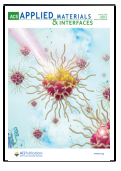

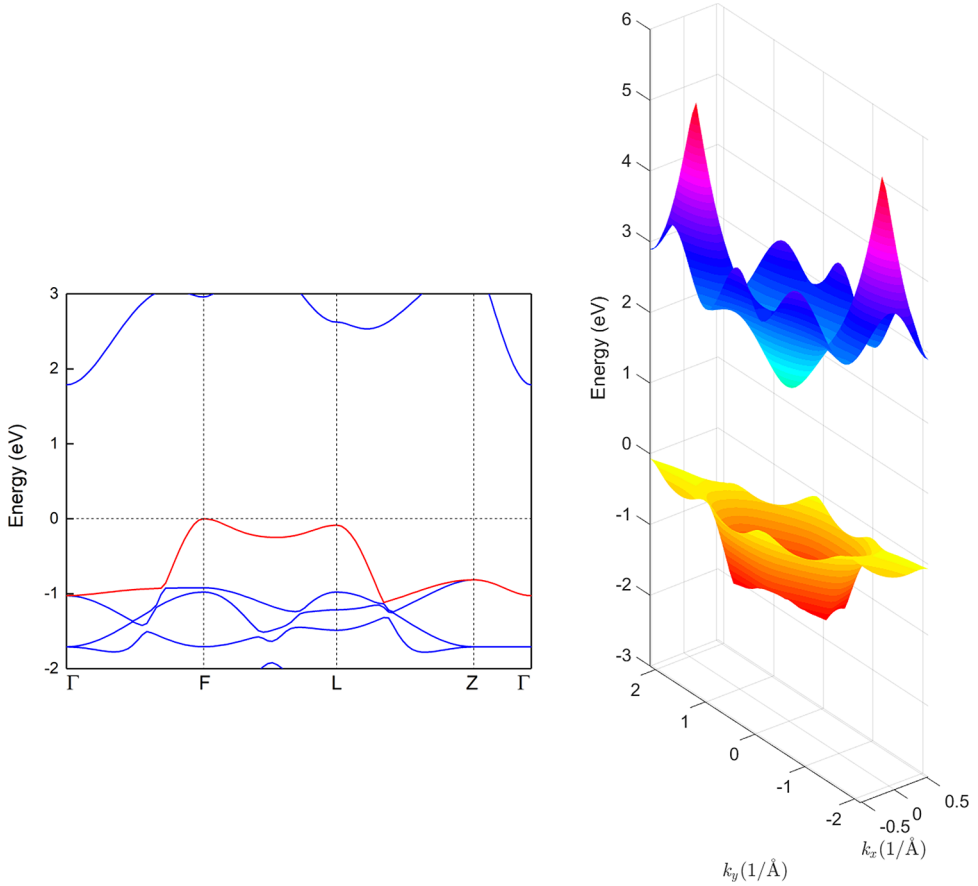

Figure 1. Two-dimensional band structure of $CuAlO_2$ unit cell, and three-dimensional band structure for the topmost valence band and the bottommost conduction band. The three-dimensional band structure is obtained using the VASPKIT code.[56] The energies refer to the valence band maximum. The high-symmetry *k*-points are Γ (0, 0, 0), *F* (0.5, 0.5, 0), *L* (0.5, 0, 0), and *Z* (0.5, 0.5, 0.5). The topmost VB is highlighted in red.

conductivity in $CuAlO_2$ has paved the way to the discovery of other p-type TCO like $CuGaO_2$ and $CuInO_2$.

In this paper, using density functional theory (DFT) calculations, we examine the effect of hole doping on the magnetic properties of $CuM^{IIIA}O_2$ with M^{IIIA} = Al, Ga, and In, having $CuAlO_2$ as a prototype material. Despite that these materials are intrinsically nonmagnetic, stable ferromagnetic phases appear for a wide range of hole densities. In addition the possibility of inducing hole doping and also ferromagnetism by cation vacancies and substitutional divalent dopants is investigated. Contrary to previous studies, we focus on doping with nonmagnetic ions. Magnetic ions typically lead to localized magnetic moments instead of ferromagnetic phases, and materials with localized magnetic moments are likely to present low spin polarization of the charge carriers, hindering their utilization in future spintronic devices. In our work, we find that nonmagnetic divalent dopants result in the emergence of ferromagnetism, and ferromagnetism can be attributed to the high-lying Cu-d states, dominating over the O-p states at the VB edge.

2. METHODS AND COMPUTATIONAL DETAILS

We perform spin-polarized DFT calculations using the Vienna Ab initio Simulation Package (VASP).[33,34] For the exchange correlation functional, the generalized gradient approximation introduced by Perdew, Burke, and Ernzerhof (PBE) is used.[35] The electron−ion interaction is described by the projector augmented wave (PAW) method.[36] For the unit cells, both the atomic positions and the volume are optimized, through the conjugate gradient method, with 10^{-8} eV energy convergence criteria and 10^{-2} eV/Å force convergence criteria. The kinetic energy cutoff is set to 600 eV, and the Brillouin zone is sampled by a 16 × 16 × 16 *k*-point grid for the atomic relaxations, whereas a 24 × 24 × 24 *k*-point grid is used for the density of states (DOS) calculations.

To achieve hole doping, we change the number of electrons of the unit cell and we add a compensating opposite charge background. Since the magnetic instabilities sensitively depend on the DOS near the Fermi level, a very dense grid of 48 × 48 × 48 *k*-points was used for the calculations of the magnetic moments. Hybrid functional calculations were also performed, using the Heyd−Scuseria−Ernzerhof (HSE) functional and the standard range-separation and mixing (0.25 Fock exchange) parameters.[37] Due to computational issues, for the hybrid functional calculations, an 8 × 8 × 8 *k*-point grid was adopted.

Finally, for the defective systems, we used supercells consisting of 192 atoms in total. The Brillouin zone was sampled by a 2 × 2 × 2 *k*-point grid for the atomic relaxations, whereas a 4 × 4 × 4 *k*-point grid was used for the DOS calculations.

3. RESULTS

3.1. Ferromagnetism in Hole-Doped $CuM^{IIIA}O_2$.

$CuAlO_2$ crystallizes in the delafossite structure (space group: $R\bar{3}m$), where each Cu atom is bonded to two O atoms forming O−Cu−O dumbbells, whereas each Al atom is bonded to six O atoms forming distorted octahedra. The Cu−O and Al−O bond lengths are found to be 1.885 and 1.925 Å, respectively, whereas for the optimized nonprimitive unit cell, the in-plane

https://doi.org/10.1021/acsami.1c00403
ACS Appl. Mater. Interfaces 2021, 13, 29770−29779

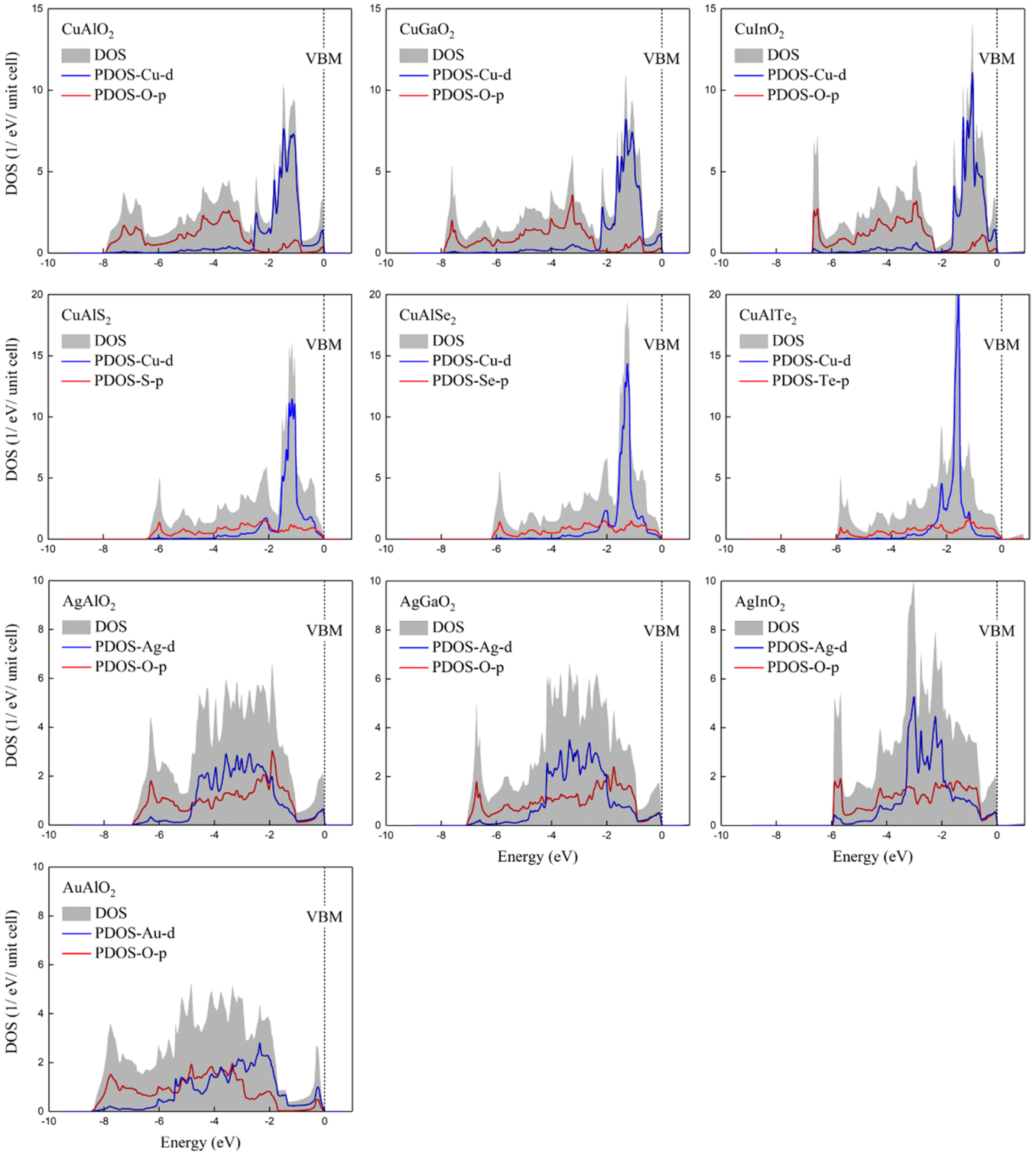

Figure 2. Total and projected valence band DOS of $CuM^{IIIA}O_2$ with M^{IIIA} = Al, Ga, and In (first-row panels), $CuAlY_2$ with Y = S, Se, and Te (second-row panels), $AgM^{IIIA}O_2$ (third-row panels), and $AuAlO_2$ (fourth-row panel). A Lorentzian broadening of 0.02 eV is used. The energies refer to the valence band maximum. The nonparticipating M^{IIIA} states are not displayed.

and out-of-plane lattice constants are $a = b = 2.880$ and $c = 17.119$ Å, in excellent agreement with experimental observations.[38] A summary of the structural parameters of $CuM^{IIIA}O_2$ with M^{IIIA} = Al, Ga, and In, in the delafossite structures is given in Table S1 in the Supporting Information. As shown in Figure 1, $CuAlO_2$ is an indirect band gap semiconductor with E_g = 1.79 eV, in agreement with previously reported DFT-PBE calculations.[39] Using HSE calculations, a gap opening of about 1.8 eV is found. The valence band (VB) top and the conduction band (CB) bottom are located at the F and Γ points, respectively, and the VB top is mainly derived from Cu-d orbitals along with a smaller contribution of O-p orbitals, as observed in Figure 2. Notably, the dispersion of the topmost VB looks like a slightly asymmetric inverted Mexican hat,

https://doi.org/10.1021/acsami.1c00403
ACS Appl. Mater. Interfaces 2021, 13, 29770−29779

where the band extrema are located at the F and L points, and the energy difference between the F and L points is 85 meV. This peculiar VB dispersion leads to a sharp high peak of the DOS near the VB edge. By shifting the Fermi level close to this peak, the Stoner criterion is fulfilled and the system becomes ferromagnetic.[40−47] Hence, hole-doped $CuAlO_2$ could be a ferromagnetic material.

To verify this assumption, we consider charged systems. Upon hole doping, a very slight shortening of the Cu−O bond lengths is observed, whereas the Al−O bond lengths present the opposite trend (see Supporting Information Figure S1). The magnetic moments and the spin polarization energies as a function of the injected holes are computed. The spin polarization energies are obtained through the equation $E_{SP} = E_{NM} - E_{FM}$, where E_{NM} and E_{FM} are the energies of the nonmagnetic and ferromagnetic phases, respectively. Using this definition, positive spin polarization energies indicate stable ferromagnetic phases. As shown in Figure 3, a ferromagnetic

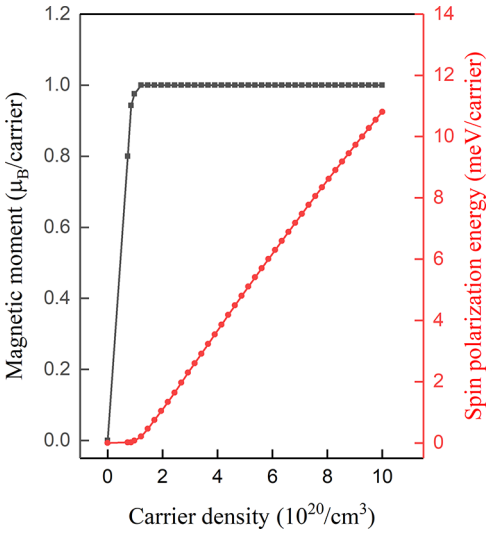

Figure 3. Carrier-dependent magnetic moment and spin polarization energy for $CuAlO_2$.

state spontaneously emerges for hole densities of ~7×10^{19}/cm^3. The magnetic moment per carrier rapidly reaches the saturation value of 1 μ_B, and it remains unchanged for hole densities up to ~1×10^{22}/cm^3. Further increase of the hole density leads to the reduction of the magnetic moment. On the other hand, the spin polarization energy per carrier strongly depends on the doping level. At the relatively low doping level, it increases by increasing the density. For $p = 6 \times 10^{21}$/cm^3, it reaches the maximum value of ~46 meV/carrier, which is larger compared to the corresponding values in similar investigations,[44,45] whereas for larger hole densities, it gradually decreases until it becomes zero. Contrary to the magnetic moment per carrier, no plateau region is observed in the spin polarization energy per carrier.

Owing to the self-interaction error, semilocal functionals tend to overdelocalize electrons, and for systems with d electrons, this can be particularly problematic. Hartree−Fock and semilocal functionals typically present an opposite self-interaction error. Thus, hybrid functionals, which use a fraction of the Hartree−Fock and a fraction of the semilocal functional, tend to reduce the self-interaction error.[48] In our work, hybrid functional calculations have been additionally performed for the hole-doped systems. Notably, using HSE calculations, the peculiar Mexican-hat-like valence band dispersion is retained and the energy difference between the F and L points is 91 meV, i.e., slightly larger compared to the PBE calculations. The magnetic properties of $CuAlO_2$ at different hole densities in the range of ~10^{19}−10^{22}/cm^3 are examined, and similar to our PBE calculations, hole-doped $CuAlO_2$ is found to be ferromagnetic. It is worth noting that the so-called pseudopotential self-interaction method (pseudo-SIC) has been widely used to eliminate self-interaction errors in standard DFT calculations.[49−51] For instance, the self-interaction-corrected electronic structures of ZnO-based DMS have been reported. Compared to those computed using standard DFT, a larger band gap and a qualitatively different description of the transition-metal d states have been observed.

As a next step, we compute the electronic band structures and the spin density plots of the charged systems. The spin density plots are obtained by the spin-up and spin-down charge density differences. As shown in Figure 4, an exchange splitting of the electronic states near the Fermi level is observed at $p = 5.0 \times 10^{20}$/cm^3. The energy difference between the spin-up and spin-down valence band maxima significantly increases, by increasing the hole density. On the other hand, we observe a shift of the Fermi level toward the lower energies. This results in a half-metallic behavior, i.e., the spin-up and spin-down states present semiconducting and metallic nature, respectively, allowing a fully polarized spin transport. The magnetization mainly arises from Cu-d orbitals along with O-p orbitals. For instance, for $p = 1 \times 10^{21}$/cm^3, the magnetization of Cu, Al, and O atoms is 86, 0, and 14% of the total magnetization, and very similar results are found for other hole densities. These results are consistent with the observation that the magnetic behavior is originated from the VB edge, which mainly consists of Cu-d states with a smaller contribution of O-p states.

Finally, we perform calculations to estimate the Curie temperature of $CuAlO_2$ at various hole densities. Our calculations are based on the mean-field evaluation of the magnetic moment by minimizing the electronic free energy of the system at specific temperatures.[52] To introduce the finite temperature, we modify the smearing factor ($\sigma = k_B T$) of the Fermi−Dirac distribution. At the relatively low doping level, the Curie temperature is below room temperature. By increasing the hole density, the Curie temperature increases, and at the high doping level, it becomes much larger than room temperature (see Supporting Information Figure S2). It should be noted that the Curie temperatures can be significantly overestimated using this approach, and the real values can be lower compared to the predicted values by as much as a factor of 2.[53]

Overall, our findings revealed that $CuAlO_2$ could be used for future spintronic devices like the spin field effect transistors (spin FETs) and the magnetic tunnel junctions (MTJs). We found that the injection of holes in $CuAlO_2$ could control/manipulate its electronic and magnetic properties. Control of magnetism through an applied voltage offers various advantages like ultralow power dissipation and reversibility, and electrically controlled ferromagnetism is highly promising for achieving optimal spintronic devices.

Besides $CuAlO_2$, other group-IIIA Cu-based oxides are examined, namely, $CuGaO_2$ and $CuInO_2$. Both $CuGaO_2$ and $CuInO_2$ present an asymmetric Mexican-hat-like VB dis-

https://doi.org/10.1021/acsami.1c00403
ACS Appl. Mater. Interfaces 2021, 13, 29770−29779

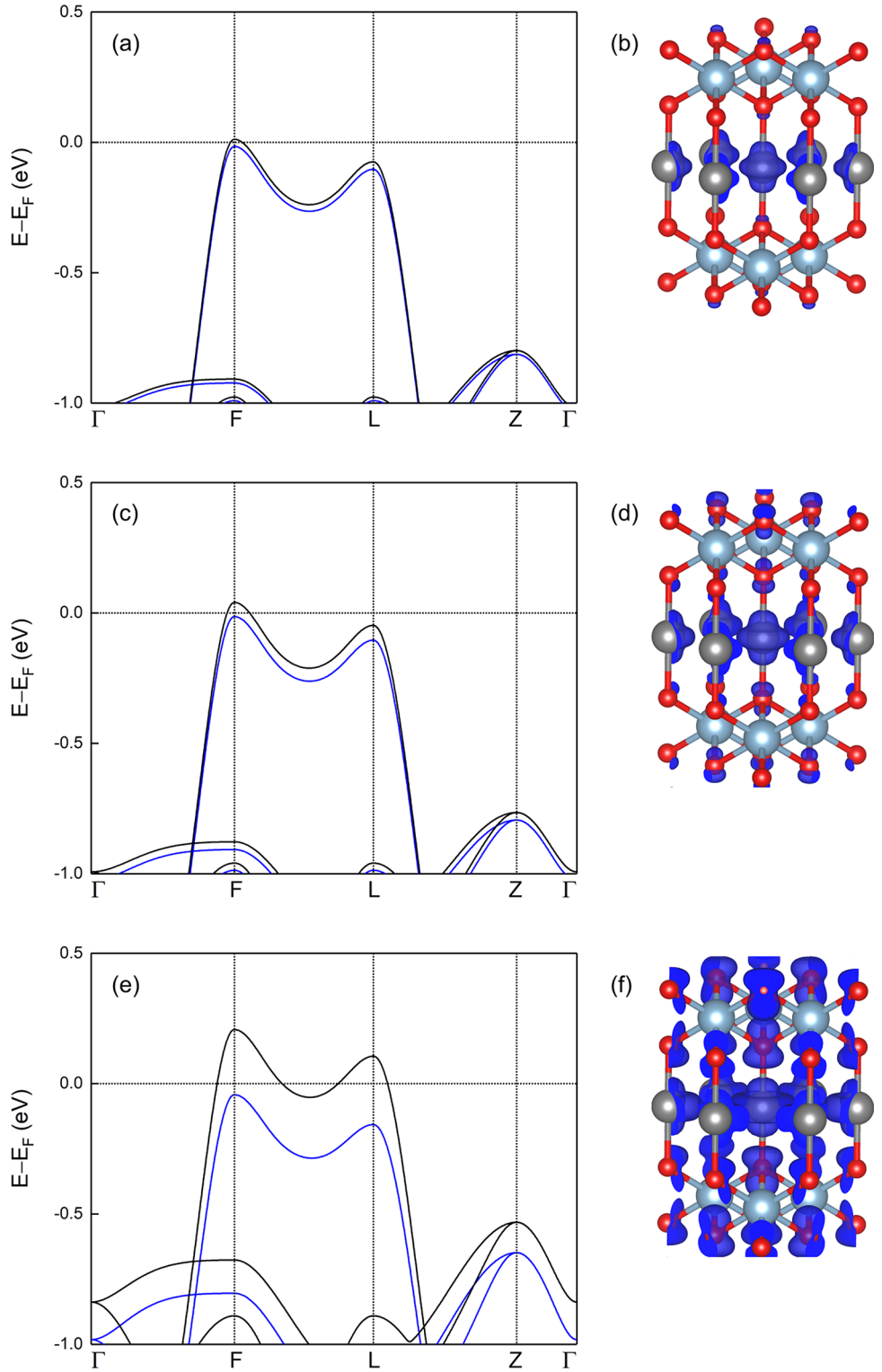

Figure 4. Electronic band structures (left) and spin density plots (right) of $CuAlO_2$ unit cells at different hole densities: (a, b) $5.0 \times 10^{20}/cm^3$, (c, d) $1.0 \times 10^{21}/cm^3$, and (e, f) $5.0 \times 10^{21}/cm^3$. The blue and black lines correspond to spin-up-like and spin-down-like states. The high-symmetry *k*-points are Γ (0, 0, 0), *F* (0.5, 0.5, 0), *L* (0.5, 0, 0), and *Z* (0.5, 0.5, 0.5). The gray, light blue, and red spheres correspond to Cu, Al, and O atoms. The isosurface is set to 0.0005 electrons per $Bohr^3$.

persion, and the energy difference between the band extrema located at the *F* and *L* points are 149 and 83 meV, respectively (see Supporting Information Figures S3 and S4). Upon hole doping, a slight shortening of the Cu−O bond lengths along with a slight elongation of the Ga−O and In−O bond lengths is observed (see Supporting Information Figure S5). A nonmagnetic-to-ferromagnetic transition occurs at $p = 1 \times 10^{20}/cm^3$ and $p = 3 \times 10^{19}/cm^3$ for Ga- and In-based compounds, respectively, and half-metallicity has been additionally observed (see Supporting Information Figures S6–

https://doi.org/10.1021/acsami.1c00403
ACS Appl. Mater. Interfaces 2021, 13, 29770−29779

S8). Both $CuGaO_2$ and $CuInO_2$ return to the nonmagnetic state for a hole density of $\sim 4 \times 10^{22}/cm^3$.

Furthermore, we examine if the corresponding chalcogenides $CuAlY_2$, where Y = S, Se, and Te, in the delafossite structures, are also promising for realizing a ferromagnetic phase upon hole doping. First, we introduce a measure for the hybridization strength between the projected orbital l of atom α and the projected orbital l′ of atom α', using the normalized cross-correlation of DOS $g(E)$

$$\gamma_{\{\alpha l\}\{\alpha' l'\}} = \frac{\int g_{\alpha l}(E) g_{\alpha' l'}(E) dE}{\sqrt{\int g^2_{\alpha l}(E) dE \int g^2_{\alpha' l'}(E) dE}} \leq 1 \quad (1)$$

In the entire VB region, the hybridization strengths between Cu-d and Y-p orbitals are found to be 0.50, 0.50, and 0.41 for $CuAlS_2$, $CuAlSe_2$, and $CuAlTe_2$, respectively, whereas the corresponding value for $CuAlO_2$ is only 0.21. In addition, contrary to the oxides where the VB edge is dominated by Cu-d states, for the sulfides and selenides, a strong hybridization of Cu-d and Y-p states is observed, whereas for tellurides, the VB edge is dominated by Te-p states, as shown in Figure 2. Thus, going from oxygen to tellurium compounds, the Cu-d character of the VB edge is found to decrease. The different nature of the VB edge in chalcogenides compared to the oxides leads to the absence of the peculiar Mexican-hat-like VB dispersion and the subsequent absence of the sharp high peak of the DOS at the VB edge. Thus, $CuAlY_2$, with Y = S, Se, and Te is expected to be nonmagnetic upon hole doping. To verify this assumption, additional calculations were performed and we found that hole doping in the range of 1×10^{19}–$1 \times 10^{22}/cm^3$ results in no magnetization in $CuAlY_2$.

$AgM^{IIIA}O_2$, where M^{IIIA} = Al, Ga, and In, as well as $AuAlO_2$ are also discussed. The hybridization strengths between Ag-d and O-p orbitals, in the entire VB region, are 0.83, 0.79, and 0.78 for M^{IIIA} = Al, Ga, and In, respectively, whereas the corresponding values for their Cu-based counterparts are only 0.21, 0.22, and 0.20. In addition, going from Cu- to Ag-based compounds, the metal-d character of the VB edge significantly decreases, leading to a less sharp peak of the DOS at the VB edge, as shown in Figure 2. Accordingly, for Ag-based compounds, the asymmetry in the Mexican-hat-like VB dispersion significantly increases and the energy differences between the band extremum located at the F and L points are 258, 428, and 340 meV for $AgAlO_2$, $AgGaO_2$, and $AgInO_2$, respectively. This should lead to a much less promising behavior of hole-doped $AgM^{IIIA}O_2$ compounds compared to $CuM^{IIIA}O_2$. Indeed, our calculations reveal that for $AgM^{IIIA}O_2$, no ferromagnetism is observed for hole densities up to $\sim 1 \times 10^{22}/cm^3$.

Interestingly, $AuAlO_2$ presents an intermediate behavior between $CuAlO_2$ and $AgAlO_2$. The hybridization strength between Au-d and O-p orbitals in the entire VB region is 0.76, whereas the VB edge has a weaker (stronger) d-character compared to $CuAlO_2$ ($AgAlO_2$), as shown in Figure 2. Furthermore, for $AuAlO_2$, the asymmetry in the Mexican-hat VB is larger (smaller) compared to $CuAlO_2$ ($AgAlO_2$) and the energy difference between the F and L points is 204 meV. We find that $AuAlO_2$ becomes ferromagnetic for only a narrow range of hole densities, i.e., $\sim 5 \times 10^{21} < p < 9 \times 10^{21}/cm^3$, and for the optimal hole density, the magnetic moment is less than 1 μ_B/carrier. A summary of the key electronic- and magnetic-related characteristics for all studied systems is shown in Table 1. A measure of the d-state strength in the VB edge is introduced using the formula

Table 1. Electronic- and Magnetic-Related Properties for All Studied Systems[a]

system	ΔE_{FL} (meV)	γ	Δ_d	$p_{NM\text{-}FM}$ (cm^{-3})
$CuAlO_2$	85	0.21	0.81	7×10^{19}
$CuGaO_2$	149	0.22	0.84	1×10^{20}
$CuInO_2$	83	0.20	0.85	3×10^{19}
$AgAlO_2$	258	0.83	0.50	
$AgGaO_2$	428	0.79	0.49	
$AgInO_2$	340	0.78	0.52	
$AuAlO_2$	204	0.76	0.68	5×10^{21}
$CuAlS_2$		0.50	0.42	
$CuAlSe_2$		0.50	0.32	
$CuAlTe_2$		0.41	0.21	

[a] ΔE_{FL} refers to the energy difference between the F and L high-symmetry k-points, γ is the hybridization strength between the metal-d and oxygen/chalcogen-p states in the VB, Δ_d is the d-state strength in the VB edge, and $p_{NM\text{-}FM}$ corresponds to the hole density, where a nonmagnetic-to-ferromagnetic transition occurs. For the estimation of $p_{NM\text{-}FM}$, calculations for hole densities up to $\sim 1 \times 10^{22}/cm^3$ are performed.

$$\Delta_d = \frac{g(\mathrm{Cu/Ag/Au - d};\, E)dE}{\int g(\mathrm{Cu/Ag/Au - d};\, E)dE + \int g(\mathrm{O/S/Se/Te - p};\, E)dE} \quad (2)$$

and for this measure, we use an integration region of 0.3 eV below the VB top.

3.2. Hole Doping Induced by Intrinsic Defects in $CuAlO_2$. As a next step, we examine the possibility of inducing hole doping and also ferromagnetism by intrinsic defects. In our study, we focus on cation vacancies (V_{Cu} and V_{Al}) in the neutral charge state. Regarding the structural properties, by removing a Cu atom, two undercoordinated O atoms are found. These atoms exhibit a slight outward relaxation by 2.1%, leading to shorter Al−O bond lengths of 1.852 Å. Accordingly, Cu atoms surrounding the missing lattice site display an outward relaxation of ∼1.3%. Contrary to Cu vacancy, which causes only a minor distortion of the lattice, Al vacancy induces a larger deformation. In particular, threefold-coordinated O atoms, neighboring the vacant site, relax outward by 10.5%, resulting in shorter Cu−O bond lengths of 1.805 Å.

We compute the defect formation energies through the equation $E_{for} = E_{tot}(CuAlO_2{:}V_A) - E_{tot}(CuAlO_2) + \mu_A$, where $E_{tot}(CuAlO_2{:}V_A)$ and $E_{tot}(CuAlO_2)$ are the energies of the defective and defect-free structures, respectively, whereas μ_A is the chemical potential of the removed cation atom, which refers to the corresponding solid structure. Cu vacancy formation energy is found to be 0.9 eV, whereas the formation energy of Al vacancy is as high as 8.4 eV, in agreement with previously reported theoretical calculations.[54]

When a Cu atom is removed, one hole is introduced in the system, whereas the removal of an Al atom corresponds to three induced holes in the system. The corresponding hole densities are about 5×10^{20} and $15 \times 10^{20}/cm^3$ for Cu- and Al-deficient systems, respectively. Cu vacancy leads to a total magnetization of 1 μ_B, whereas Al vacancy results in a total

https://doi.org/10.1021/acsami.1c00403
ACS Appl. Mater. Interfaces 2021, 13, 29770−29779

magnetic moment of 3 μ_B, which is equivalent to the number of holes. For the case of Cu vacancy, the local magnetic moments of the nearest-neighboring Cu sites are ~0.05 μ_B, whereas all other Cu sites present nonzero magnetic moments up to 0.04 μ_B. In addition, the total Cu, Al, and O magnetizations are found to be ~0.9, 0.0, and 0.1 μ_B, respectively. At the same hole concentration, for the hole-injected $CuAlO_2$, the Cu, Al, and O magnetizations are also 90, 0, and 10% of the total magnetization, respectively. Next, the relaxation effect on the magnetic properties is investigated. In agreement with the previous results, the unrelaxed defective structure has a total magnetic moment of 1 μ_B and the distribution of the local magnetic moments is very similar. Figure 5 shows the spin density plots for both vacancy defects.

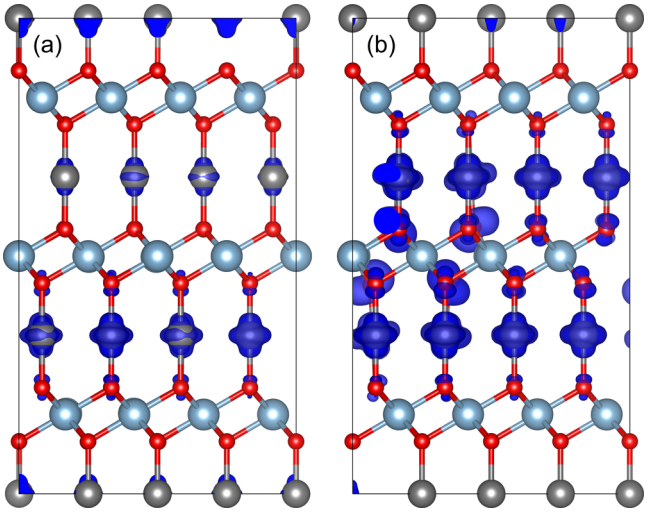

Figure 5. Spin density plots of (a) Cu-deficient and (b) Al-deficient $CuAlO_2$. The isosurface is 0.001 electrons per $Bohr^3$.

The spin polarization energies of Cu- and Al-deficient systems are found to be ~7 and 93 meV, respectively, and the positive values reveal that the ferromagnetic phases are favorable compared to the nonmagnetic phases. Test calculations for singly negatively charged Cu vacancies and triply negatively charged Al vacancies are also performed. The charged defective systems are found to be nonmagnetic, confirming that the induced holes are responsible for the emergence of ferromagnetism.

Regarding the electronic properties, Figure 6 shows the DOS of the defective $CuAlO_2$. For both cation vacancies, no deep gap states are observed. Due to the induced holes, the Fermi level is shifted within the VB, leading to an asymmetry between the spin-up and spin-down states, and both systems are found to be half-metals. Obviously, the Fermi-level shift for the Al-deficient system is larger compared to the Cu-deficient one.

3.3. Hole Doping Induced by Extrinsic Defects in $CuAlO_2$. Next, we study the substitution of Al atoms by group-IIA and group-IIB atoms, namely, X = Mg, Ca, Zn, and Cd. Note that Al atoms have three valence electrons, whereas group-IIA and group-IIB have only two valence electrons. Thus, these substitutional dopants are attractive alternatives for inducing hole doping and also ferromagnetism in $CuAlO_2$. Concerning the structural properties, oxygens surrounding the Mg, Ca, Zn, and Cd dopants display an outward relaxation of ~6.1, 14.1, 8.0, and 14.8%, resulting in elongated Mg−O, Ca−O, Zn−O, and Cd−O bond lengths of 2.04, 2.20, 2.08, and 2.21 Å, respectively. We compute the dopant formation energies through the equation $E_{for} = E_{tot}(CuAlO_2{:}X) - E_{tot}(CuAlO_2) + \mu_{Al} - \mu_X$, where $E_{tot}(CuAlO_2{:}X)$ and $E_{tot}(CuAlO_2)$ are the energies of the doped and undoped structures, whereas μ_{Al} and μ_X are the chemical potentials of Al and dopant atoms, respectively, which refer to the corresponding solid structures. The formation energies are found to be 1.7, 2.8, 4.8, and 6.7 eV for Mg-, Ca-, Zn-, and Cd-doped systems, respectively.

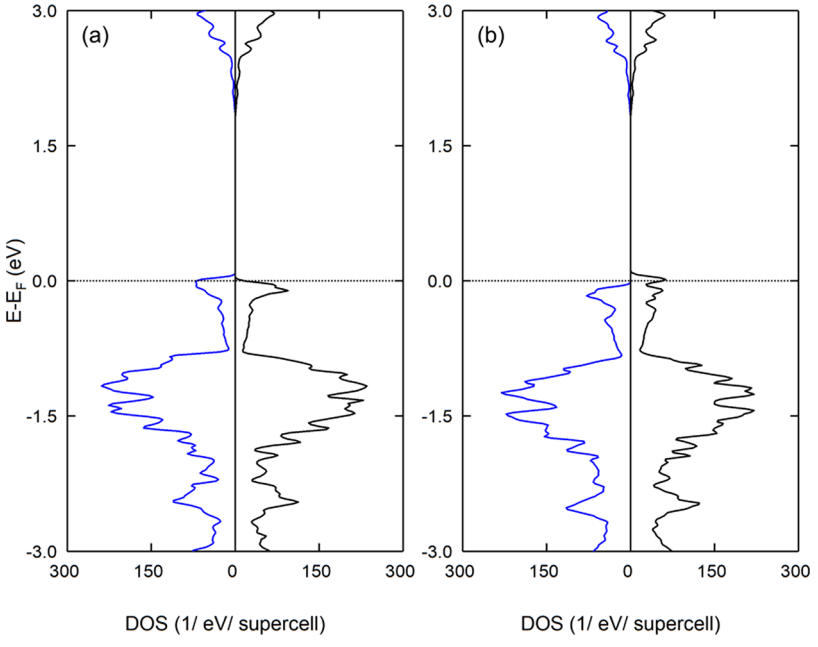

Figure 6. DOS of (a) Cu-deficient and (b) Al-deficient $CuAlO_2$. A Lorentzian broadening of 0.02 eV is used. The blue and black lines correspond to spin-up-like and spin-down-like DOS.

https://doi.org/10.1021/acsami.1c00403
ACS Appl. Mater. Interfaces 2021, 13, 29770−29779

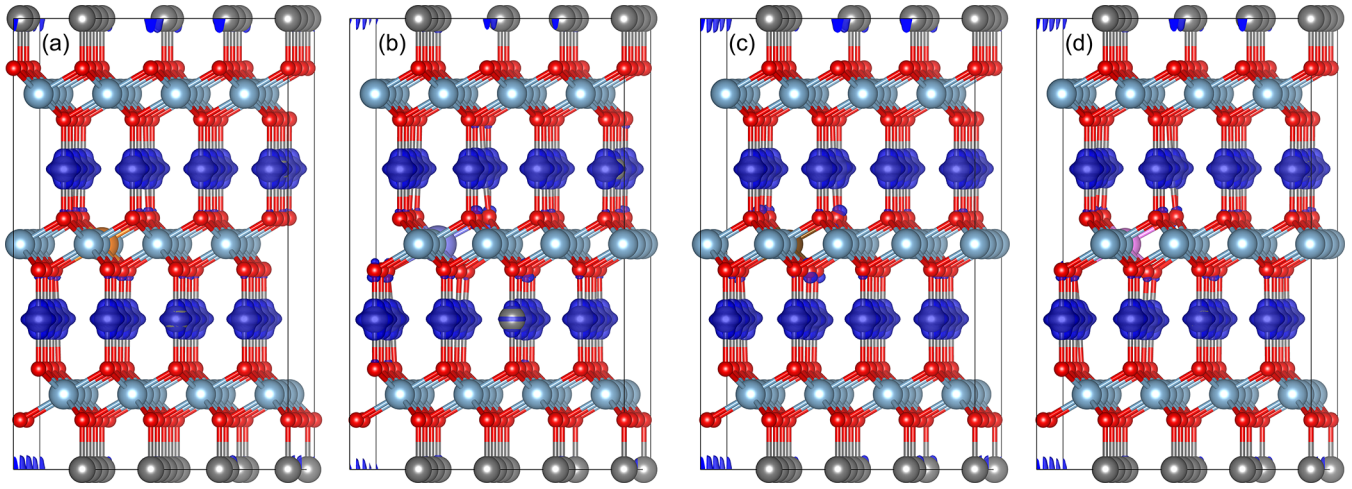

Figure 7. Spin density plots of doped $CuAlO_2$ (a) Mg-on-Al site, (b) Ca-on-Al site, (c) Zn-on-Al site, and (d) Cd-on-Al site. The orange, purple, brown, and pink spheres correspond to Mg, Ca, Zn, and Cd atoms. The isosurface is set to 0.001 electrons per $Bohr^3$.

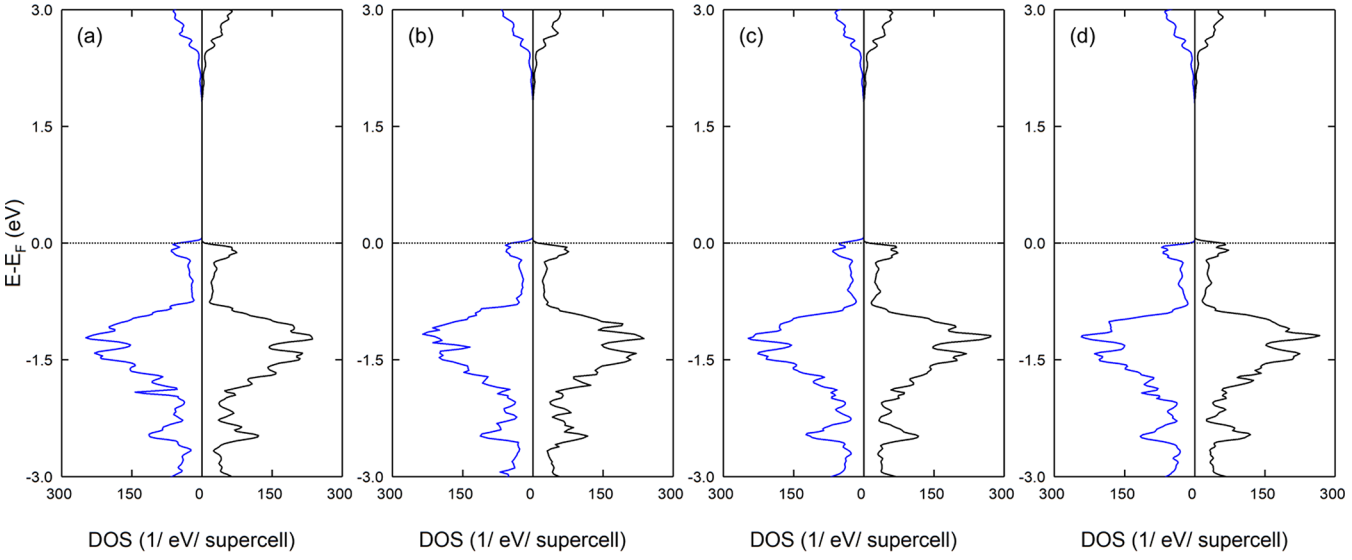

Figure 8. DOS of doped $CuAlO_2$ (a) Mg-on-Al site, (b) Ca-on-Al site, (c) Zn-on-Al site, and (d) Cd-on-Al site. A Lorentzian broadening of 0.02 eV is used. The blue and black lines correspond to spin-up-like and spin-down-like DOS.

Taking Mg-doped $CuAlO_2$ as an example, the total magnetic moment is found to be 1 μ_B, i.e., equivalent to the number of holes. The 32 Cu atoms, which sandwich the dopant-containing Al plane, present local magnetic moments of about 0.02−0.04μ_B, whereas the remaining 16 Cu atoms present negligible magnetic moments. Magnetization is found to be less localized in plane, compared to the out-of-plane direction. The total Cu and O magnetizations are found to be ∼ 0.9 and 0.1 μ_B, respectively, whereas the dopant atom and all Al atoms have zero magnetic moments. Remarkably, our findings are different from those reported in similar investigations, where the magnetic moments are found to be strongly localized in the impurity atoms.[44] Our theoretical calculations are also in good agreement with recent experimental observations, where $CuAl_{1-x}Mg_xO_2$ with x = 0.05 is found to be ferromagnetic at room temperature.[55] Similar results are also obtained for the magnetic moments for the other group-IIA- and group-IIB-doped systems, and their spin density plots are shown in Figure 7. For all doped systems, positive spin polarization energies are found and their values are 7.2, 6.3, 7.3, and 7.2 meV for Mg, Ca, Zn, and Cd dopants, respectively. Concerning the electronic properties, no deep gap states are observed, and an obvious shift of the Fermi level within the VB along with half-metallicity is observed, as shown in Figure 8.

4. CONCLUSIONS

Using density functional theory calculations, we examined the electronic and magnetic properties of $CuM^{IIIA}O_2$ with M^{IIIA} = Al, Ga, and In, upon hole doping. Our simulations revealed a nonmagnetic-to-ferromagnetic transition for the hole-doped systems. Ferromagnetism arises from an exchange splitting of the electronic states at the valence band edge, and it can be attributed to the high-lying Cu-d states dominating over the O-p states. Besides ferromagnetism, half-metallicity has been additionally observed, i.e., the spin-up and spin-down states present semiconducting and metallic behavior, respectively, allowing a fully polarized spin transport. The possibility of inducing hole doping and a subsequent ferromagnetic order by cation vacancies was also investigated. We found that Cu

https://doi.org/10.1021/acsami.1c00403
ACS Appl. Mater. Interfaces 2021, 13, 29770−29779

vacancy presents a formation energy lower than 1 eV and leads to a total magnetization of 1 μ_B. The local magnetic moments of the nearest-neighboring Cu sites are ~0.05 μ_B, whereas all other Cu sites present nonzero magnetic moments up to 0.04 μ_B. Besides cation vacancies, group-IIA and group-IIB atoms replacing Al atoms were examined. Interestingly, these nonmagnetic divalent dopants also result in the emergence of ferromagnetism.

■ ASSOCIATED CONTENT

Supporting Information

The Supporting Information is available free of charge at https://pubs.acs.org/doi/10.1021/acsami.1c00403.

Bond length variations for hole-doped $CuM^{IIIA}O_2$; temperature-dependent magnetic moment for $CuAlO_2$; band structures of $CuGaO_2$ and $CuInO_2$; carrier dependent magnetic moment and spin polarization energy for $CuGaO_2$ and $CuInO_2$; band structures of hole-doped $CuGaO_2$ and $CuInO_2$; and structural properties of $CuM^{IIIA}O_2$ (PDF)

■ AUTHOR INFORMATION

Corresponding Author

Konstantina Iordanidou − *Centre for Materials Science and Nanotechnology, Department of Physics, University of Oslo, 0316 Oslo, Norway;* orcid.org/0000-0003-4696-8204; Email: konstantina.iordanidou@smn.uio.no

Author

Clas Persson − *Centre for Materials Science and Nanotechnology, Department of Physics, University of Oslo, 0316 Oslo, Norway;* orcid.org/0000-0002-9050-5445

Complete contact information is available at: https://pubs.acs.org/10.1021/acsami.1c00403

Notes

The authors declare no competing financial interest.

■ ACKNOWLEDGMENTS

Fruitful discussions with Prof. Michel Houssa (KU Leuven) are gratefully acknowledged. This work was financially supported by the Research Council of Norway (ToppForsk project: 251131). Part of this work was supported by computational time at NSC, Linköping University, granted from the Swedish National Infrastructure for Computing (SNIC). The authors acknowledge access to HPC resources provided by UNINETT Sigma2—the National Infrastructure for High Performance Computing and Data Storage in Norway.

■ REFERENCES

(1) Wolf, S. A.; Awschalom, D. D.; Buhrman, R. A.; Daughton, J. M.; von Molnár, V. S.; Roukes, M. L.; Chtchelkanova, A. Y.; Treger, D. M. Spintronics: A Spin-Based Electronics Vision for the Future. *Science* **2001**, *294*, 1488−1495.

(2) Furdyna, J. K. Diluted Magnetic Semiconductors. *J. Appl. Phys.* **1988**, *64*, R29−R64.

(3) De Jonge, W. J. M.; Swagten, H. J. M. Magnetic Properties of Diluted Magnetic Semiconductors. *J. Magn. Magn. Mater.* **1991**, *100*, 322−345.

(4) Sarma, S. D.; Hwang, E. H.; Kaminski, A. Temperature-Dependent Magnetization in Diluted Magnetic Semiconductors. *Phys. Rev. B* **2003**, *67*, No. 155201.

(5) Sato, K.; Bergqvist, L.; Kudrnovský, J.; Dederichs, P. H.; Eriksson, O.; Turek, I.; Sanyal, B.; Bouzerar, G.; Katayama-Yoshida, H.; Dinh, V. A.; Fukushima, T.; et al. First-Principles Theory of Dilute Magnetic Semiconductors. *Rev. Mod. Phys.* **2010**, *82*, 1633.

(6) Matsumoto, Y.; Murakami, M.; Shono, T.; Hasegawa, T.; Fukumura, T.; Kawasaki, M.; Ahmet, P.; Chikyow, T.; Koshihara, S. Y.; Koinuma, H. Room-Temperature Ferromagnetism in Transparent Transition Metal-Doped Titanium Dioxide. *Science* **2001**, *291*, 854−856.

(7) Matsumoto, Y.; Takahashi, R.; Murakami, M.; Koida, T.; Fan, X. J.; Hasegawa, T.; Fukumura, T.; Kawasaki, M.; Koshihara, S. Y.; Koinuma, H. Ferromagnetism in Co-Doped TiO_2 Rutile Thin Films Grown by Laser Molecular Beam Epitaxy. *Jpn. J. Appl. Phys.* **2001**, *40*, L1204−L1206.

(8) Wang, Z.; Wang, W.; Tang, J.; Tung, L. D.; Spinu, L.; Zhou, W. Extraordinary Hall Effect and Ferromagnetism in Fe-Doped Reduced Rutile. *Appl. Phys. Lett.* **2003**, *83*, 518−520.

(9) Ogale, S. B.; Choudhary, R. J.; Buban, J. P.; Lofland, S. E.; Shinde, S. R.; Kale, S. N.; Kulkarni, V. N.; Higgins, J.; Lanci, C.; Simpson, J. R.; Browning, N. D.; et al. High Temperature Ferromagnetism with a Giant Magnetic Moment in Transparent Co-doped $SnO_{2-\delta}$. *Phys. Rev. Lett.* **2003**, *91*, No. 077205.

(10) Buchholz, D. B.; Changm, R. P. H.; Song, J. H.; Ketterson, J. B. Room-Temperature Ferromagnetism in Cu-Doped ZnO Thin Films. *Appl. Phys. Lett.* **2005**, *87*, No. 082504.

(11) Venkatesan, M.; Fitzgerald, C. B.; Coey, J. M. D. Unexpected Magnetism in a Dielectric Oxide. *Nature* **2004**, *430*, No. 630.

(12) Ghosh, S.; Khan, G. G.; Mandal, K.; Samanta, A.; Nambissan, P. M. G. Evolution of Vacancy-Type Defects, Phase Transition, and Intrinsic Ferromagnetism During Annealing of Nanocrystalline TiO_2 Studied by Positron Annihilation Spectroscopy. *J. Phys. Chem. C* **2013**, *117*, 8458−8467.

(13) Yi, J. B.; Lim, C. C.; Xing, G. Z.; Fan, H. M.; Van, L. H.; Huang, S. L.; Yang, K. S.; Huang, X. L.; Qin, X. B.; Wang, B. Y.; Wu, T.; Wang, L.; Zhang, H. T.; Gao, X. Y.; Liu, T.; Wee, A. T. S.; Feng, Y. P.; Ding, J. Ferromagnetism in Dilute Magnetic Semiconductors through Defect Engineering: Li-Doped ZnO. *Phys. Rev. Lett.* **2010**, *104*, No. 137201.

(14) Martínez-Boubeta, C.; Beltrán, J. I.; Balcells, L.; Konstantinović, Z.; Valencia, S.; Schmitz, D.; Arbiol, J.; Estrade, S.; Cornil, J.; Martínez, B. Ferromagnetism in Transparent Thin Films of MgO. *Phys. Rev. B* **2010**, *82*, No. 024405.

(15) Srivastava, S. K.; Lejay, P.; Barbara, B.; Pailhès, S.; Madigou, V.; Bouzerar, G. Possible Room-Temperature Ferromagnetism in K-Doped SnO_2: X-Ray Diffraction and High-Resolution Transmission Electron Microscopy Study. *Phys. Rev. B* **2010**, *82*, No. 193203.

(16) Yang, K.; Dai, Y.; Huang, B.; Whangbo, M. H. On the Possibility of Ferromagnetism in Carbon-Doped Anatase TiO_2. *Appl. Phys. Lett.* **2008**, *93*, No. 132507.

(17) Yang, K.; Dai, Y.; Huang, B.; Whangbo, M. H. Density Functional Studies of the Magnetic Properties in Nitrogen Doped TiO_2. *Chem. Phys. Lett.* **2009**, *481*, 99−102.

(18) Yang, K.; Wu, R.; Shen, L.; Feng, Y. P.; Dai, Y.; Huang, B. Origin of d^0 Magnetism in II-VI and III-V Semiconductors by Substitutional Doping at Anion Site. *Phys. Rev. B* **2010**, *81*, No. 125211.

(19) Kenmochi, K.; Ann Dinh, V.; Sato, K.; Yanase, A.; Katayama-Yoshida, H. Materials Design of Transparent and Half-Metallic Ferromagnets of MgO, SrO and BaO without Magnetic Elements. *J. Phys. Soc. Jpn.* **2004**, *73*, 2952−2954.

(20) Kenmochi, K.; Seike, M.; Sato, K.; Yanase, A.; Katayama-Yoshida, H. New Class of Diluted Ferromagnetic Semiconductors Based on CaO without Transition Metal Elements. *Jpn. J. Appl. Phys.* **2004**, *43*, L934.

(21) Kemmochi, K.; Seike, M.; Sato, K.; Yanase, A.; Katayama-Yoshida, H. New Class of High-Tc Diluted Ferromagnetic Semiconductors Based on CaO without Transition Metal Elements. *J. Supercond.* **2005**, *18*, 37−40.

(22) Sato, K.; Bergqvist, L.; Kudrnovský, J.; Dederichs, P. H.; Eriksson, O.; Turek, I.; Sanyal, B.; Bouzerar, G.; Katayama-Yoshida, H.; Dinh, V. A.; Fukushima, T.; et al. First-Principles Theory of Dilute Magnetic Semiconductors. *Rev. Mod. Phys.* **2010**, *82*, 1633.
(23) Sato, K.; Katayama-Yoshida, H.; Dederichs, P. H. Dilute Magnetic Semiconductors. *Psi-k Newsl.* **2005**, *70*, 93−110.
(24) Kizaki, H.; Sato, K.; Yanase, A.; Katayama-Yoshida, H. Ab Initio Calculations of $CuAlO_2$-Based Dilute Magnetic Semiconductor. *Phys. B* **2006**, *376*−*377*, 812−815.
(25) Chen, C.; Dong, C.; Wang, B.; Huang, J.; Wang, Y. Synthesis and Room Temperature Ferromagnetism in Fe-Doped $CuAlO_2$ Semiconductor. *J. Wuhan Univ. Technol., Mater. Sci. Ed.* **2013**, *28*, 500−503.
(26) Dong, C. J.; Yu, W. X.; Xu, M.; Cao, J. J.; Zhang, Y.; Chuai, Y. H.; Wang, Y. D. Evidence of Room Temperature Ferromagnetism in Co-Doped Transparent $CuAlO_2$ Semiconductor. *J. Alloys Compd.* **2012**, *512*, 195−198.
(27) Kizaki, H.; Sato, K.; Yanase, A.; Katayama-Yoshida, H. First-Principles Materials Design of $CuAlO_2$ Based Dilute Magnetic Semiconducting Oxide. *Jpn. J. Appl. Phys.* **2005**, *44*, L1187−L1189.
(28) Bandara, J.; Yasomanee, J. P. P-Type Oxide Semiconductors as Hole Collectors in Dye-Sensitized Solid-State Solar Cells. *Semicond. Sci. Technol.* **2007**, *22*, 20−24.
(29) Zheng, X. G.; Taniguchi, K.; Takahashi, A.; Liu, Y.; Xu, C. N. Room Temperature Sensing of Ozone by Transparent p-Type Semiconductor $CuAlO_2$. *Appl. Phys. Lett.* **2004**, *85*, 1728−1729.
(30) Ahmed, J.; Blakely, C. K.; Prakash, J.; Bruno, S. R.; Yu, M.; Wu, Y.; Poltavets, V. V. Scalable Synthesis of Delafossite $CuAlO_2$ Nanoparticles for p-Type Dye-Sensitized Solar Cells Applications. *J. Alloys Compd.* **2014**, *591*, 275−279.
(31) Kawazoe, H.; Yasukawa, M.; Hyodo, H.; Kurita, M.; Yanagi, H.; Hosono, H. P-Type Electrical Conduction in Transparent Thin Films of $CuAlO_2$. *Nature* **1997**, *389*, 939−942.
(32) Zhang, K. H.; Xi, K.; Blamire, M. G.; Egdell, R. G. P-Type Transparent Conducting Oxides. *J. Phys.: Condens. Matter* **2016**, *28*, No. 383002.
(33) Kresse, G.; Furthmüller, J. Efficient Iterative Schemes for Ab Initio Total-Energy Calculations Using a Plane-Wave Basis Set. *Phys. Rev. B* **1996**, *54*, 11169−11186.
(34) Kresse, G.; Furthmüller, J. Efficiency of Ab-Initio Total Energy Calculations for Metals and Semiconductors Using a Plane-Wave Basis Set. *Comput. Mater. Sci.* **1996**, *6*, 15−50.
(35) Perdew, J. P.; Burke, K.; Ernzerhof, M. Generalized Gradient Approximation Made Simple. *Phys. Rev. Lett.* **1996**, *77*, 3865−3868.
(36) Blöchl, P. E. Projector Augmented-Wave Method. *Phys. Rev. B* **1994**, *50*, 17953−17979.
(37) Heyd, J.; Scuseria, G. E.; Ernzerhof, M. Hybrid Functionals Based on a Screened Coulomb Potential. *J. Chem. Phys.* **2003**, *118*, 8207−8215.
(38) Ishiguro, T.; Kitazawa, A.; Mizutani, N.; Kato, M. Single-Crystal Growth and Crystal Structure Refinement of $CuAlO_2$. *J. Solid State Chem.* **1981**, *40*, 170−174.
(39) Yanagi, H.; Inoue, S. I.; Ueda, K.; Kawazoe, H.; Hosono, H.; Hamada, N. Electronic Structure and Optoelectronic Properties of Transparent p-Type Conducting $CuAlO_2$. *J. Appl. Phys.* **2000**, *88*, 4159−4163.
(40) Meng, R.; Houssa, M.; Iordanidou, K.; Pourtois, G.; Afanas'ev, V. V.; Stesmans, A. Two-Dimensional Gallium and Indium Oxides from Global Structure Searching: Ferromagnetism and Half Metallicity via Hole Doping. *J. Appl. Phys.* **2020**, *128*, No. 034304.
(41) Meng, R.; Houssa, M.; Iordanidou, K.; Pourtois, G.; Afanas'ev, V. V.; Stesmans, A. Ferromagnetism and Half-Metallicity in Two-Dimensional MO (M=Ga,In) Monolayers Induced by Hole Doping. *Phys. Rev. Mater.* **2020**, *4*, No. 074001.
(42) Houssa, M.; Meng, R.; Iordanidou, K.; Pourtois, G.; Afanas'ev, V. V.; Stesmans, A. Doping-Induced Ferromagnetism in InSe and SnO Monolayers. *J. Comput. Electron.* **2021**, *20*, 88−94.
(43) Houssa, M.; Meng, R.; Iordanidou, K.; Pourtois, G.; Afanas'ev, V. V.; Stesmans, A. Stoner Ferromagnetism in Two-Dimensional Materials. *ECS Trans.* **2019**, *92*, 35−41.
(44) Iordanidou, K.; Houssa, M.; Persson, C. Carrier-Mediated Ferromagnetism in Two-Dimensional PtS_2. *RSC Adv.* **2020**, *10*, 952−957.
(45) Iordanidou, K.; Houssa, M.; Kioseoglou, J.; Afanas'ev, V. V.; Stesmans, A.; Persson, C. Hole-Doped 2D InSe for Spintronic Applications. *ACS Appl. Nano Mater.* **2018**, *1*, 6656−6665.
(46) Houssa, M.; Iordanidou, K.; Pourtois, G.; Afanas'ev, V. V.; Stesmans, A. Ferromagnetism in two-dimensional hole-doped SnO. *AIP Adv.* **2018**, *8*, No. 055010.
(47) Houssa, M.; Iordanidou, K.; Pourtois, G.; Afanas'ev, V. V.; Stesmans, A. Hole-Doping Induced Ferromagnetism in Monolayer SnO: A First-Principles Study. *ECS Trans.* **2017**, *80*, 339−345.
(48) Janesko, B. G.; Henderson, T. M.; Scuseria, G. E. Screened Hybrid Density Functionals for Solid-State Chemistry and Physics. *Phys. Chem. Chem. Phys.* **2009**, *11*, 443−454.
(49) Toyoda, M.; Akai, H.; Sato, K.; Katayama-Yoshida, H. Electronic Structures of (Zn, TM) O (TM: V, Cr, Mn, Fe, Co, and Ni) in the Self-Interaction-Corrected Calculations. *Phys. B* **2006**, *376*−*377*, 647−650.
(50) Toyoda, M.; Akai, H.; Sato, K.; Katayama-Yoshida, H. Curie Temperature of GaMnN and GaMnAs from LDA-SIC Electronic Structure Calculations. *Phys. Status Solidi C* **2006**, *3*, 4155−4159.
(51) An Dinh, V.; Toyoda, M.; Sato, K.; Katayama-Yoshida, H. Exchange Interaction and T C in Alkaline-Earth-Metal-Oxide-Based DMS without Magnetic Impurities: First Principle Pseudo-SIC and Monte Carlo Calculation. *J. Phys. Soc. Jpn.* **2006**, *75*, No. 093705.
(52) Cao, T.; Li, Z.; Louie, S. G. Tunable Magnetism and Half-Metallicity in Hole-Doped Monolayer GaSe. *Phys. Rev. Lett.* **2015**, *114*, No. 236602.
(53) Ashcroft, N. W.; Mermin, N. D. *Solid State Physics*; Holt Rinehart/Winston: New York, 1976.
(54) Kumar, M.; Zhao, H.; Persson, C. Study of Band-Structure, Optical Properties and Native Defects in $A^IB^{III}O_2$ (A^I = Cu or Ag, B^{III} = Al, Ga or In) Delafossites. *Semicond. Sci. Technol.* **2013**, *28*, No. 065003.
(55) Agrawal, S.; Parveen, A.; Azam, A. Influence of Mg on Structural, Electrical and Magnetic Properties of $CuAlO_2$ Nanoparticles. *Mater. Lett.* **2016**, *168*, 125−128.
(56) Wang, V.; Xu, N.; Liu, J. C.; Tang, G.; Geng, W. T. Vaspkit: A User-Friendly Interface Facilitating High-Throughput Computing and Analysis Using Vasp Code, arXiv:1908.08269. arXiv.org e-Print archive. https://arxiv.org/abs/1908.08269 (accessed Aug 22, 2019).

https://doi.org/10.1021/acsami.1c00403
ACS Appl. Mater. Interfaces 2021, 13, 29770−29779